Crystallographic and Magnetic Structure of the Perovskite-Type Compound BaFeO$_{2.5}$: Unrivaled Complexity in Oxygen Vacancy Ordering

Oliver Clemens,*,[†,‡] Melanie Gröting,[§] Ralf Witte,[†,‡] J. Manuel Perez-Mato,[∥] Christoph Loho,[†] Frank J. Berry,[#] Robert Kruk,[‡] Kevin S. Knight,[⊥] Adrian J. Wright,[#] Horst Hahn,[†,‡] and Peter R. Slater[#]

[†]Joint Research Laboratory Nanomaterials and [§]Fachgebiet Materialmodellierung, Technische Universität Darmstadt, Jovanka-Bontschits-Straße 2, 64287 Darmstadt, Germany

[‡]Institute of Nanotechnology, KIT, Hermann-von-Helmholtz-Platz 1, 76344 Eggenstein-Leopoldshafen, Germany

[∥]Departamento de Física de la Materia Condensada, Facultad de Ciencia y Tecnología, Universidad del País Vasco (UPV/EHU), Apartado 644, 48080 Bilbao, Spain

[⊥]ISIS Facility, Rutherford Appleton Laboratory, Harwell Oxford, Didcot OX11 0QX, United Kingdom

[#]School of Chemistry, The University of Birmingham, Birmingham B15 2TT, United Kingdom

S *Supporting Information*

ABSTRACT: We report here on the characterization of the vacancy-ordered perovskite-type structure of BaFeO$_{2.5}$ by means of combined Rietveld analysis of powder X-ray and neutron diffraction data. The compound crystallizes in the monoclinic space group $P2_1/c$ [$a = 6.9753(1)$ Å, $b = 11.7281(2)$ Å, $c = 23.4507(4)$ Å, $\beta = 98.813(1)°$, and $Z = 28$] containing seven crystallographically different iron atoms. The coordination scheme is determined to be Ba$_7$(FeO$_{4/2}$)$_1$(FeO$_{3/2}$O$_{1/1}$)$_3$(FeO$_{5/2}$)$_2$(FeO$_{6/2}$)$_1$ = Ba$_7$Fe$^{[6]}_1$Fe$^{[5]}_2$Fe$^{[4]}_4$O$_{17.5}$ and is in agreement with the ^{57}Fe Mössbauer spectra and density functional theory based calculations. To our knowledge, the structure of BaFeO$_{2.5}$ is the most complicated perovskite-type superstructure reported so far (largest primitive cell, number of ABX$_{2.5}$ units per unit cell, and number of different crystallographic sites). The magnetic structure was determined from the powder neutron diffraction data and can be understood in terms of "G-type" antiferromagnetic ordering between connected iron-containing polyhedra, in agreement with field-sweep and zero-field-cooled/field-cooled measurements.
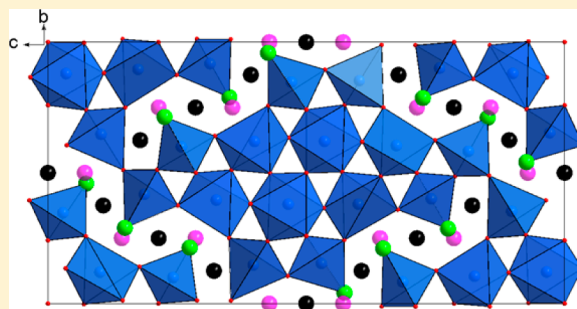
1. INTRODUCTION

Perovskite-type compounds have many applications, ranging from electrode materials in solid oxide fuel cells (e.g., La$_{1-x}$Sr$_x$CoO$_{3-d}$[1] and La$_{1-x}$Sr$_x$FeO$_{3-d}$[2,3]), ferroelectrics (e.g., BaTiO$_3$[4]), multiferroics (e.g., BiFeO$_3$, Bi$_{1-x}$A$_x$FeO$_{3-d}$, with A = Ba, Sr, Ca, Pb[5−11]) to materials with interesting magnetic properties [e.g., ferromagnetic BaFeO$_3$[12] (by oxidation of BaFeO$_{2.5}$ using O$_3$) compared with antiferromagnetic BaFeO$_2$F compounds[13−15]]. The possibility of vacancies on the anion sublattice gives rise to many of the properties of such compounds, including ionic (anionic) conductivity (facilitated by anion vacancies), electronic conductivity (due to mixed valence), and magnetic order, which is often promoted via superexchange interactions via the anions. In addition, the ordering of vacancies can give rise to polar crystal structures (polar space group *Ima*2), which are often found in brownmillerite-type compounds ABO$_{2.5}$ (or alternatively written as A$_2$B$_2$O$_5$ and named after the mineral brownmillerite Ca$_2$Fe$^{[6]}$Al$^{[4]}$O$_5$,[16] with [6] and [4] = coordination number, CN).

Vacancy ordering for ABO$_{2.5}$ "cubic perovskite"-type compounds (i.e., ccp arrangement of the AO$_3$ layers) is most often achieved by adopting this brownmillerite structure. The symmetry relationship between the cubic perovskite and brownmillerite can be well understood in terms of group− subgroup relationships (e.g., see 17). In the brownmillerite-type structure, the B-site cation is found in octahedral and tetrahedral coordination (ratio 1:1, with layered ordering of the differently coordinated B-site ions) and the structure can be found in a large variety of compounds, including SrFeO$_{2.5}$,[18] CaFeO$_{2.5}$,[19] BaInO$_{2.5}$,[20] SrCoO$_{2.5}$,[21] and Ca$_2$MnGaO$_5$.[22] However, other superstructures are also known, showing square instead of tetrahedral coordination as well as square-pyramidal coordination of the B-site cations.[23,24] Because such anion-deficient perovskites are of interest for a wide range of applications, clarification of the different types of anion vacancy ordering is important because, even for systems that appear

cubic by diffraction techniques, local vacancy ordering may occur.

The anion-deficient phase $BaFeO_{2.5}$ is the subject of investigation in this work and is important because it has been reported to adopt a different vacancy-ordered "cubic perovskite"-type modification, the nature of which is currently not fully understood. Initial structural investigations[25] on this compound have been shown to be incorrect, and a variety of techniques [among them Mössbauer spectroscopy, high-resolution electron microscopy (HREM), and crystallographic image processing (CIP)[26−28]] have subsequently been used to investigate the crystallographic structure of $BaFeO_{2.5}$. Using electron diffraction, Parras et al.[26,27] managed to index their data in the monoclinic space group $P2_1/c$, with lattice parameters of $a = 7.05(1)$ Å, $b = 11.71(1)$ Å, $c = 23.40(1)$ Å, and $\beta = 98.3(1)°$ with 28 formula units of $BaFeO_{2.5}$ per unit cell. Mössbauer spectroscopy data[27] were interpreted in terms of the structure, which was assumed to contain seven crystallographically different Fe^{3+} ions resulting in a coordination scheme of $Ba_7Fe^{[6]}_3Fe^{[5]}_1Fe^{[4]}_3O_{17.5}$ and which, in principle, is in agreement with a general site multiplicity of 4 for $P2_1/c$. Attempts to investigate the explicit order of vacancies were performed by HREM and CIP experiments[28] and helped to reveal a general pattern for this ordering. However, the reported structure was described in such a way that all of the atoms were located on "ideal sites" derived from the cubic prototype, leaving out distinct oxygen ions without allowing shifts from the ideal positions.

In their article from 1990, Parras et al. observed that, "In any case neutron diffraction experiments are highly necessary."[27] In this article, we describe a detailed investigation of the crystallographic structure by means of a coupled Rietveld analysis of powder X-ray and neutron diffraction (NPD) data to clarify the real vacancy ordering and resulting iron coordination geometries for this compound, and we also interpret our Mössbauer spectroscopy data by comparison with that reported previously.[27] To our knowledge (and we have compared a large variety of such superstructures reported in reviews on this topic[21,22]), the structure of $BaFeO_{2.5}$ reported here is the most complicated perovskite-type superstructure reported so far (largest primitive cell, number of $ABX_{2.5}$ units, and number of different crystallographic sites). In addition, we report on the magnetic structure, which agrees well with the magnetic characterization from SQUID measurements, and we additionally describe the results of density functional theory (DFT)-based calculations as well as group theoretical considerations revealing the structural relationship to the cubic perovskite structure.

2. EXPERIMENTAL SECTION

2.1. Sample Preparation. $BaFeO_{2.5}$ was prepared as reported in ref 27. Stoichiometric amounts of $BaCO_3$ (Sigma-Aldrich, ≥99%) and Fe_2O_3 (Fluka, ≥99%) were ground using a planetary ball mill (300 rpm, 15 min) and twice heated at 1100 °C for 15 h under flowing N_2 with one intermediate grinding. It must be noted that contact of the sample with CO_2-[29,30] and H_2O-containing[31] atmospheres must be avoided after preparation because $BaFeO_{2.5}$ is not stable as a result of water incorporation into the anion vacancies.

2.2. Diffraction Experiments. Powder X-ray diffraction (XRD) patterns were recorded on a Bruker D8 diffractometer with Bragg−Brentano geometry and a fine-focus X-ray tube with a copper anode. No primary beam monochromator was attached. A VANTEC detector and a variable divergence slit were used. The total scan time was 17 h for the angular range between $2\theta = 5$ and $130°$.

Time-of-flight (TOF) NPD data were recorded on the HRPD high-resolution diffractometer at the ISIS pulsed spallation source (Rutherford Appleton Laboratory, Didcot, U.K.). A total of 4 g of powdered $BaFeO_{2.5}$ was loaded into 8-mm-diameter thin-walled cylindrical vanadium sample cans, and data were collected at ambient temperature for a 130 μAh proton beam current to the ISIS target (corresponding to ~3.5 h of beamtime).

The initial refinement of the nuclear structure using both the XRD and NPD data was performed using the Rietveld method with the program *TOPAS 4.2* (Bruker AXS, Karlsruhe, Germany).[32] For the room temperature XRD data, the whole 2θ range was used, while for the NPD data, only those data collected in the highest-resolution backscattering detector bank (bank 1, average $2\theta = 168.329°$, and d_{max} ~ 2.5 Å) were used. The instrumental intensity distribution for the X-ray data was determined empirically from a sort of fundamental parameter set,[33] using a reference scan of LaB_6, and the microstructural parameters were refined to adjust the peak shapes for the XRD data. For the NPD data, a corresponding TOF shape model was used. The lattice parameters were constrained to be the same for neutron and XRD data, and the same positional parameters were used and refined for both data sets. Independent thermal displacement parameters were refined for each type of atom. While these parameters were also constrained to be the same for both powder XRD and NPD data, an additional B overall value was refined for XRD data accounting for further effects such as absorption or surface roughness. Reflections that showed a large magnetic scattering contribution were omitted from the initial crystallographic refinement.

Refinement of the magnetic structure of $BaFeO_{2.5}$ was performed with the program *TOPAS Academic 5*[32,34] using the NPD data collected in all of the HRPD detector banks 1−3 at room temperature. A magnetic propagation vector of $[^1/_2, 0, 0]$ was indicated from Pawley fits of the pattern, and this vector is compatible with a G-type arrangement of the magnetic moments. This G-type arrangement was then tested and verified by introducing a second phase with a doubled a axis for which only the magnetic scattering was calculated and using constraints belonging to a G-type setting, thus allowing only refinement of an overall magnitude and an overall orientation of the magnetic moment without differing between different crystallographic iron sites. Unit cell, atomic position, and thermal vibration parameters in this second phase were set to the refined values determined from the coupled analysis of bank 1 and XRD data. Different starting orientations of the magnetic moment in this G-type arrangement were investigated and evaluated, and from this, the correct magnetic symmetry and space group (P_a2_1/c) were derived, indicating that the M_y component is virtually zero. Other magnetic symmetries that are, in principle, also compatible with a space group of P_a2_1/c and the **k** vector of $[^1/_2, 0, 0]$ were also tested and could be ruled out.

For the final analysis of the diffraction data, both the nuclear and magnetic structure parameters were refined at once using the as-determined magnetic symmetry with space group P_a2_1/c and $M_y = 0$ (the symmetry relationships are provided in detail in the Supporting Information, SI); the XRD and NPD data of all of the detector banks were used for this analysis. For refinement of the magnetic structure, the amount of constraints was lowered, allowing for different magnitudes and orientations of the magnetic moments on different crystallographic sites. For refinement of the nuclear structure, the same constraints as those described above were used. Structural parameters given in this article refer to this final analysis.

2.3. Magnetometric Measurements. Direct-current (dc) susceptibility measurements were performed over the temperature range 5−390 K using a Quantum Design MPMS-XL SQUID magnetometer. The sample was precooled to 5 K in zero magnetic field and then in an applied magnetic field μ_0H of 20 mT. The susceptibility was subsequently measured while warming the sample up to 390 K (zero-field-cooled, ZFC) and then cooling it again in the applied magnetic field to 5 K (field-cooled, FC). Field-dependent dc susceptibility measurements were performed on the same instrument at 5 and 390 K between 0 and 4.5 T.

2.4. Mössbauer Measurements. The ^{57}Fe Mössbauer spectrum for $BaFeO_{2.5}$ was recorded in standard transmission geometry in
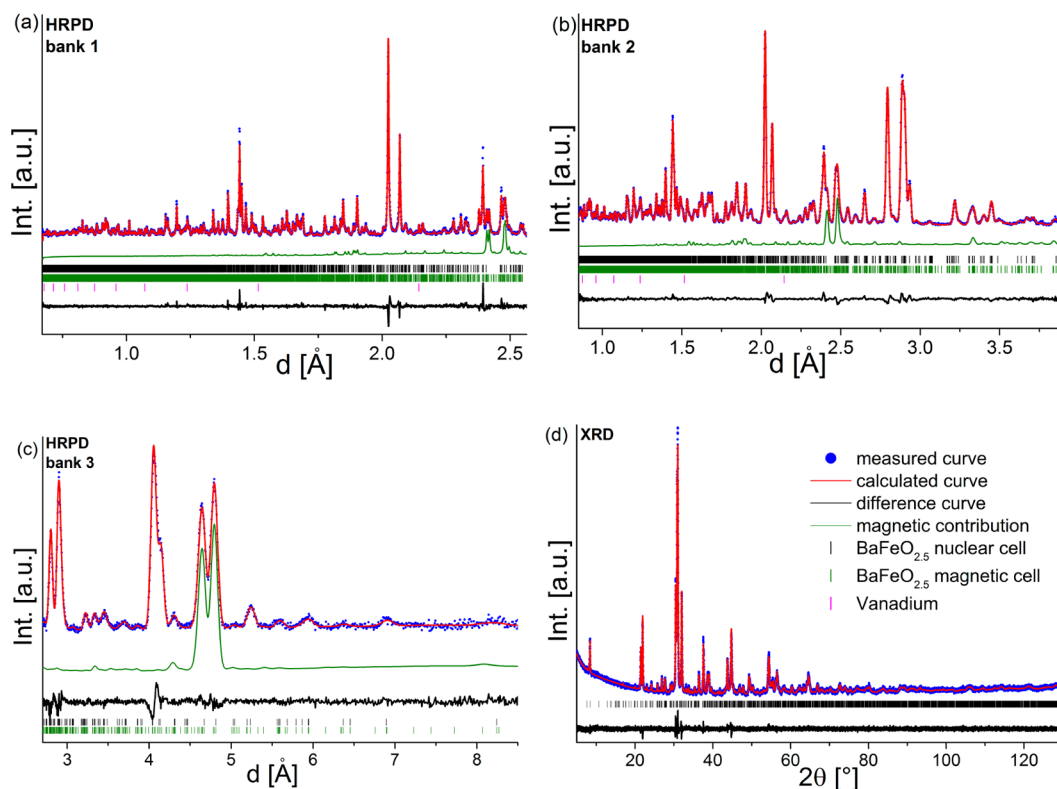
Figure 1. Coupled Rietveld analysis of the nuclear and magnetic structure of $BaFeO_{2.5}$ of HRPD bank 1 (a), bank 2 (b), and bank 3 (c) and XRD data (d).

constant acceleration mode using a ca. 15 mCi ^{57}Co/Rh source at room temperature. The data are computed using *WinNormos* software by R. A. Brand (WISSEL company).[35] All isomer shifts are quoted relative to metallic iron at room temperature.

2.5. Computational Method. For the DFT calculations, the Vienna Ab-initio Simulation Package (*VASP*, version 5.3) was used.[36−39] Projector augmented plane waves (PAW)[40] were applied with the spin-polarized GGA-PBE exchange correlation functional.[41] Because of the already large unit cell size, the magnetic order was restricted to ferromagnetic. The valence electron configurations of the PAW data sets were Ba $5s^25p^66s^2$, Fe $3s^23p^64s^23d^6$, and O $2s^22p^4$.

For the Fe 3d electrons, an additional Hubbard U parameter was introduced. The LSDA+U calculations were performed in the formulation of Dudarev et al.[42] with $U − J$ = 4 eV, as was used for Fe^{3+} in the multiferroic perovskite $BiFeO_3$.[43] The plane-wave energy cutoff was set to 600 eV, and a 6 × 4 × 2 Monkhorst−Pack k-point mesh was used for Brillouin zone integration. The crystal structure (lattice parameters and atomic positions) was relaxed at a fixed unit cell volume (the experimental value) until residual forces were less than 0.01 eV/A. The partial density of states (pDOS) were calculated by integrating the charge density over spheres of the ionic radii[44] around each ion (Ba^{2+} 1.45 Å, Fe^{3+} 0.55 Å, and $O^{2−}$ 1.35 Å).

2.6. Scanning Electron Microscopy (SEM) and Energy-Dispersive X-ray Spectroscopy (EDX). The SEM images were taken using the secondary electron detector of a Philips XL30 FEG scanning electron microscope operating at 30 keV. For EDX analysis, the EDAX Genesis system was used and an energy resolution of about 140 eV was applied. The mapped area was on the order of 100 μm^2, and the barium-to-iron ratio was determined from the Ba L and Fe K lines. The sample was sputtered with approximately 10 nm of gold prior to the measurements.

3. RESULTS AND DISCUSSION

3.1. Structural Analysis. The structural model of Zou et al.[28] was used as a starting model for refinement of the crystal structure of $BaFeO_{2.5}$. In agreement with the magnetic

characterization reported in section 3.3, we could conclude that their proposed space group $P2_1/c$ is likely to be correct and is consistent with the (001) and (010) reflections found in the XRD data at ∼8°. Because of the high number of parameters for this refinement [7 Ba, 7 Fe, and 17 O ions on the general site 4c (x, y, z) and only 1 O at a special site 2a], constraints were used for the thermal parameters (same thermal parameter for each type of atom). A coupled analysis of XRD and NPD data is beneficial in such cases where strong X-ray scatterers (e.g., transition metals and heavy alkaline earths) are found adjacent to light X-ray scatterers (e.g., O and F).[14,15,45] The initial coupled Rietveld analysis of XRD and NPD data (relaxing all positional parameters from the starting model of Zou et al.[28]) generally gave a good description for the intensities of most of the superstructure reflections, but some of them showed significant misfit. This misfit could be attributed to the incorrect allocation of three different oxygen ions due to strong correlation for the refinement because the fit of the XRD data was superior to the one of the NPD data. Therefore, a Fourier difference analysis was performed on the NPD data, which assisted in identifying the correct positions for these three oxygen ions. Those ions were therefore placed at the positions indicated from the Fourier difference analysis, and the refinement then resulted in a pattern of vacancy distribution similar to that observed by Zou et al.[28] but also showing strong tilt and/or rotation of the iron coordination polyhedra and a different coordination scheme of the iron atoms (see later in this section). The final coupled Rietveld analysis (including the magnetic contribution; see section 3.3) is in excellent agreement with the observed patterns and is shown in Figure 1; the refined structural parameters are listed in Table 1.

To verify the structural model, we also attempted to build different starting models (by reallocating some of the oxygen

Table 1. Crystal Structure of BaFeO$_{2.5}$ (Space Group $P2_1/c$) from the Final Coupled Rietveld Analysis of XRD and NPD Data

atom	Wyckoff site	x	y	z	occupancy	B [Å^2]
Ba^{2+}	Ba1/4c	0.0546(9)	0.3517(6)	0.1145(3)	1	0.55(4)
Ba^{2+}	Ba2/4c	0.2500(10)	0.6141(6)	0.3283(3)	1	0.55(4)
Ba^{2+}	Ba3/4c	0.1431(9)	0.1304(6)	0.3215(3)	1	0.55(4)
Ba^{2+}	Ba4/4c	0.3257(10)	0.6328(5)	0.0379(4)	1	0.55(4)
Ba^{2+}	Ba5/4c	0.0547(11)	0.6176(7)	0.6001(4)	1	0.55(4)
Ba^{2+}	Ba6/4c	0.5603(10)	0.3549(6)	0.2558(3)	1	0.55(4)
Ba^{2+}	Ba7/4c	0.3544(13)	0.1102(5)	0.0364(4)	1	0.55(4)
Fe^{3+}	Fe1/4c	0.5249(8)	0.3531(5)	0.1038(3)	1	0.47(3)
Fe^{3+}	Fe2/4c	0.3848(8)	0.5816(4)	0.1860(3)	1	0.47(3)
Fe^{3+}	Fe3/4c	0.0620(9)	0.3996(5)	0.2595(3)	1	0.47(3)
Fe^{3+}	Fe4/4c	0.1739(10)	0.1525(5)	0.4707(3)	1	0.47(3)
Fe^{3+}	Fe5/4c	0.4359(9)	0.3817(5)	0.3988(3)	1	0.47(3)
Fe^{3+}	Fe6/4c	0.2707(9)	0.1045(5)	0.1746(3)	1	0.47(3)
Fe^{3+}	Fe7/4c	0.1458(11)	0.6217(4)	0.4644(4)	1	0.47(3)
O^{-2}	O1/2a	0	0	0	1	0.66(2)
O^{-2}	O2/4c	0.2972(13)	0.7097(8)	0.1485(4)	1	0.66(2)
O^{-2}	O3/4c	−0.0628(13)	0.2770(8)	0.2271(4)	1	0.66(2)
O^{-2}	O4/4c	0.0382(14)	0.0449(7)	0.4273(4)	1	0.66(2)
O^{-2}	O5/4c	0.0080(14)	0.2474(9)	0.0021(5)	1	0.66(2)
O^{-2}	O6/4c	0.2954(15)	0.5000(9)	0.4297(5)	1	0.66(2)
O^{-2}	O7/4c	0.7133(14)	0.2597(9)	0.0766(4)	1	0.66(2)
O^{-2}	O8/4c	0.0559(15)	0.1195(10)	0.1079(5)	1	0.66(2)
O^{-2}	O9/4c	0.4060(15)	−0.0138(9)	0.1436(5)	1	0.66(2)
O^{-2}	O10/4c	0.4063(13)	0.2443(8)	0.1470(5)	1	0.66(2)
O^{-2}	O11/4c	0.1173(15)	0.0036(10)	0.2168(5)	1	0.66(2)
O^{-2}	O12/4c	0.4500(14)	0.1263(9)	0.2497(5)	1	0.66(2)
O^{-2}	O13/4c	0.1944(16)	0.4907(10)	0.2110(5)	1	0.66(2)
O^{-2}	O14/4c	0.5416(13)	0.4917(8)	0.1449(4)	1	0.66(2)
O^{-2}	O15/4c	0.3115(14)	0.2406(10)	0.4261(5)	1	0.66(2)
O^{-2}	O16/4c	0.3596(16)	0.3923(7)	0.0364(6)	1	0.66(2)
O^{-2}	O17/4c	0.2515(16)	0.3583(8)	0.3225(5)	1	0.66(2)
O^{-2}	O18/4c	0.653(2)	0.3669(7)	0.4636(6)	1	0.66(2)
a [Å]		6.9753(1)	c [Å]	23.4507(4)	V [Å^3]	1895.39(5)
b [Å]		11.7281(2)	β [deg]	98.813(1)		
R_{wp} (XRD + NPD) [%]		7.67	GOF (XRD + NPD)	6.00	R_{Bragg} [%]	1.28 (XRD), 2.32 (NPD bank 1)

ions to different vacancies), but the refinements always converged back to the reported structural model or gave a significantly worse description of the neutron pattern. We also failed to find evidence for significant partial occupancy of the anion sites. Such a refinement is highly critical because of a high correlation of parameters for this complicated structure.

In addition, EDX analysis (see the SI) was performed and confirmed within experimental error the Ba/Fe ratio of 1:1 (experimentally 1.035:1). This, together with the Mössbauer experiments (reported in section 3.2) showing only the presence of Fe^{3+}, gives clear evidence that the compound has a composition of BaFeO$_{2.5}$ (Ba$_2$Fe$_2$O$_5$).

SEM images further showed that the sample is a homogeneous powder with grain sizes of ∼5−10 μm (see the SI). In their HREM analysis, Zou et al.[28] reported that they observed a simple hexagonal pattern only "at the thinnest areas near the edge" of the particles (up to a maximum of a couple of nanometers; however, we think that this could also be affected by the uptake of small amounts of water[31]) and that the monoclinic structure with space group $P2_1/c$ represents the crystallites otherwise (>100 nm). We could confirm this by estimating the degree of crystallinity (see the SI), and those experiments indicate that the sample can be assumed to be represented by the monoclinic structure with space group $P2_1/c$

to close to 100% within errors. The actual crystallite size determined from reflection broadening of the XRD patterns is about 1 order of magnitude smaller (∼150−200 nm), indicating the presence of domain walls within the grains. However, Rietveld analysis also indicates that strain has an additional influence on the broadening of the reflections, making the separation of both effects extremely difficult via a fundamental parameter technique and nearly impossible via the Williamson−Hall method because of strong peak overlap. Despite the presence of domain walls, the fact that the sample contains only Fe^{3+} (see Mössbauer section 3.2), in combination with the principle of local charge neutrality and the excellent fit of the diffraction patterns, indicates that the oxygen content and vacancy distribution is likely to be equal and homogeneous between different domains.

The bond distances and formal CNs of the respective cations are given in Table 2, and drawings of the coordination polyhedra of the different iron sites are shown in Figure 2a−g. The structure was shown to be in good agreement with calculations of the bond valence sums (BVSs), giving a global instability index of 0.2 and a relatively good description of the valences of the different ions (see Table 3), although we acknowledge that BVSs can be problematic for perovskite compounds.[46,47] The fact that some of the values of the BVSs

Table 2. M−O Bond Distances (Å) and Formal CNs for Ba1−7 and Fe1−7[a]

Ba1 (CN = 9)		Ba2 (CN = 10)		Ba3 (CN = 10)		Ba4 (CN = 10)		Ba5 (CN = 10)		Ba6 (CN = 10)		Ba7 (CN = 12)	
O4	2.51(1)	O3	2.55(1)	O14	2.75(1)	O18	2.75(1)	O1	2.70(1)	O12	2.79(1)	O6	2.77(1)
O7	2.64(1)	O6	2.70(1)	O17	2.78(1)	O5	2.76(1)	O18	2.71(1)	O9	2.80(1)	O6	2.79(1)
O8	2.73(1)	O7	2.79(1)	O11	2.85(1)	O2	2.78(1)	O2	2.77(1)	O11	2.84(1)	O1	2.80(1)
O10	2.76(1)	O8	2.80(1)	O15	2.86(1)	O16	2.83(1)	O9	2.79(1)	O17	2.85(1)	O18	2.85(1)
O13	2.84(1)	O9	2.82(1)	O4	2.87(1)	O15	2.84(1)	O8	2.79(1)	O2	2.87(1)	O8	2.87(1)
O5	2.88(1)	O10	2.83(1)	O13	2.87(1)	O7	2.94(1)	O6	2.80(1)	O10	2.92(1)	O9	2.88(1)
O3	3.01(1)	O11	2.92(1)	O12	2.92(1)	O4	2.97(1)	O5	2.82(2)	O3	2.96(1)	O18	2.90(1)
O16	3.05(1)	O12	2.99(1)	O3	2.99(1)	O16	3.02(1)	O17	3.02(1)	O14	3.04(1)	O5	2.91(1)
O14	3.74(1)	O17	3.00(1)	O2	3.38(1)	O14	3.19(1)	O15	3.03(1)	O13	3.05(1)	O10	3.00(1)
		O13	3.08(1)	O2	3.97(1)	O4	3.67(1)	O11	3.06(1)	O12	3.19(1)	O7	3.08(1)
												O15	3.10(1)
												O16	3.31(1)

Fe1 (CN = 4)		Fe2 (CN = 4)		Fe3 (CN = 4)		Fe4 (CN = 4)		Fe5 (CN = 5)		Fe6 (CN = 5)		Fe7 (CN = 6)	
O16	1.87(1)	O2	1.80(1)	O3	1.79(1)	O4	1.80(1)	O6	1.90(1)	O9	1.89(1)	O1	2.01(1)
O14	1.88(1)	O12	1.83(1)	O17	1.89(1)	O15	1.84(1)	O18	1.98(2)	O11	1.96(1)	O6	2.01(1)
O7	1.89(1)	O13	1.87(1)	O11	1.89(1)	O5	1.88(1)	O9	2.01(1)	O8	2.00(1)	O18	2.03(1)
O10	1.90(1)	O14	1.89(1)	O13	1.90(1)	O16	1.93(1)	O15	2.02(1)	O12	2.01(1)	O8	2.03(2)
								O17	2.06(1)	O10	2.05(1)	O5	2.05(1)
												O7	2.19(1)
O3	*3.86(1)*	*O4*	*3.68(1)*	*O9*	*4.17(1)*	*O4*	*3.79(1)*	*O2*	*3.07(1)*	*O3*	*3.45(1)*		

[a]For the barium ions, only oxygen ions with $d < 4$ Å have been considered. For iron atoms with CN lower than 6, another next-nearest oxygen, which should not be considered to be bonded, is given.
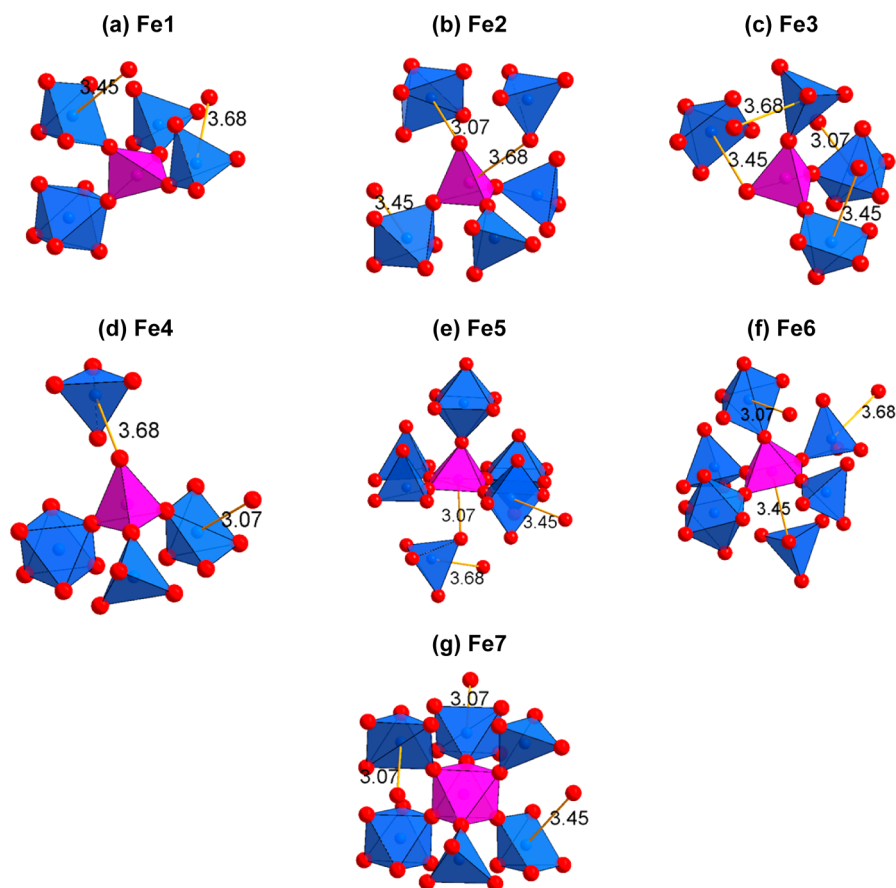

Figure 2. Local coordination of the seven crystallographically different iron sites and connectivity to neighboring polyhedra.

for iron are smaller than 3 might be consistent with the sensitivity of the compound toward uptake of water[31] and/or CO_2[29,30] (allowing for the formation of additional Fe−O bonds), which might then allow for structural relaxation and more stable local environments. In addition, all of the O−O distances are in agreement with the minimum distance expected from ionic radii [2.70 Å from Shannon radii[44] compared to the lowest distance found for the pair O11−O12 of 2.74(1) Å].

Table 3. BVSs for the Different Crystallographic Sites in Monoclinic BaFeO$_{2.5}$^{a}

site	BVS	site	BVS	site	BVS	site	BVS
Ba1	2.06	Fe1	2.66	O1	2.05	O10	1.90
Ba2	2.23	Fe2	2.94	O2	1.63	O11	1.94
Ba3	1.73	Fe3	2.79	O3	1.74	O12	1.92
Ba4	1.81	Fe4	2.84	O4	1.69	O13	2.00
Ba5	2.21	Fe5	2.61	O5	1.99	O14	1.86
Ba6	1.82	Fe6	2.67	O6	2.14	O15	1.90
Ba7	2.15	Fe7	2.69	O7	1.84	O16	1.86
				O8	1.94	O17	1.85
				O9	2.05	O18	1.95

^{a}The global instability index was calculated to be 0.20.

The structure contains seven crystallographically different iron atoms, for which the effective coordination numbers (ECoNs)[48] have been calculated and are shown in Table 4.

Table 4. ECoNs[48] for the Different Barium and Iron Ions

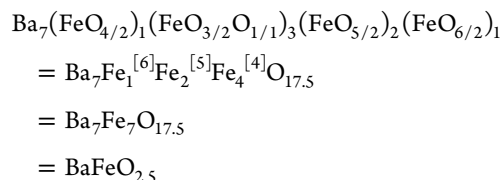| site	ECoN	site	ECoN
Ba1	6.41	Fe1	4.00
Ba2	8.41	Fe2	3.95
Ba3	8.10	Fe3	3.89
Ba4	8.30	Fe4	3.89
Ba5	9.20	Fe5	4.86
Ba6	9.31	Fe6	4.82
Ba7	10.86	Fe7	5.81

Four of these iron atoms (Fe1−4) are found in tetrahedral coordination. The tetrahedron of Fe1 (see Figure 2a) properly shares its corners with other iron coordination polyhedra. In contrast, Fe2−4 (see Figure 2b−d) share only three of their corners with other iron coordination polyhedra. Their fourth corner is not shared with other polyhedra, and the large distance to a neighboring iron atom precludes consideration as a coordinating polyhedron (distances of 3.07, 3.45, and 3.68 Å). This was confirmed by BVSs, which showed that a Fe−O distance of 3.07 Å only gives an additional charge increment of ∼0.05 and is also confirmed by considering the ECoNs of the cations. In addition, this is expressed by the shape of the polyhedra in which the "freestanding oxygen ions" point outward. Furthermore, very long additional bonds ($d > 3.6$ Å) are found for Fe2−4 (exemplarily shown for Fe2; see Figure 2b), which again should not be considered to contribute to bonding from ECoN calculations and BVSs. Furthermore, the nonshared oxygen ions connected to Fe4 and Fe3 (O4 and O3) show relatively short bond distances of 2.51 and 2.55 Å to the neighboring Ba ions, Ba1 and Ba2.

The Fe5 and Fe6 sites (see Figure 2e,f) are found in 5-fold square-pyramidal coordination. Again, for both Fe5 and Fe6, an additional very long bond is formed to another neighboring

tetrahedron (Fe2 and Fe3) with bond distances of 3.07 and 3.45 Å, increasing the coordination to a pseudooctahedron. However, Fe5 and Fe6 show a clear off-center shift to the corner opposite to the long-distance bond, which is very typical for square-pyramidal coordination.

The Fe7 site (see Figure 2g) was found in a slightly distorted octahedral coordination. The atom is connected to the oxygen located at the special position 2a and is therefore connected to another polyhedron of Fe7.

In conclusion, the coordination scheme is in agreement with the composition BaFeO$_{2.5}$ and can be described by the following formula/coordination scheme

$$Ba_7(FeO_{4/2})_1(FeO_{3/2}O_{1/1})_3(FeO_{5/2})_2(FeO_{6/2})_1$$
$$= Ba_7Fe_1{}^{[6]}Fe_2{}^{[5]}Fe_4{}^{[4]}O_{17.5}$$
$$= Ba_7Fe_7O_{17.5}$$
$$= BaFeO_{2.5}$$

Although this scheme is in contrast to that proposed by Parras et al. (which had been derived from Mössbauer data only[27]) and Zou et al.,[28]

$$Ba_7Fe_3{}^{[6]}Fe_1{}^{[5]}Fe_3{}^{[4]}O_{17.5}$$
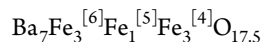
we will show in section 3.2 that the Mössbauer data of Parras et al.[27] are in agreement with our own recorded data but can be interpreted to be in excellent agreement with the structure described in this article and with Mössbauer spectroscopy data from similar Fe^{3+}-containing compounds.

Additionally, the vacancy-ordered monoclinic structure of BaFeO$_{2.5}$ can be understood in terms of a group−subgroup relationship derived from the ideal cubic perovskite structure. This symmetry tree is described in more detail in the SI; however, a shortened scheme showing the essential structural relationship is shown in Figure 3. This symmetry relationship could, in principle, help to elucidate how topochemical reactions,[17] which can be used to transform the compound into cubic-perovskite-type BaFeO$_3$[12] and BaFeO$_2$F[13,49,50] (also altering the magnetic properties), can work from a structural point of view.

The approximate positions of the vacancies (the four vacant oxygen positions derived from the "undistorted" cubic structure are given in the SI) appear to order in a rhombic-type pattern in the bc plane (see Figure 4a). This principal pattern was also observed by Zou et al. using HREM and CIP measurements[28] and can therefore be confirmed by our investigations. Upon closer examination of the structure in comparison to the pseudocubic setting, we found that O2, O3, and O4 showed by far the strongest shift from their ideal positions (mainly along the a axis), whereas all of the other oxygen ions remained far closer to their positions for a pseudocubic arrangement (see Figure 4b,c).
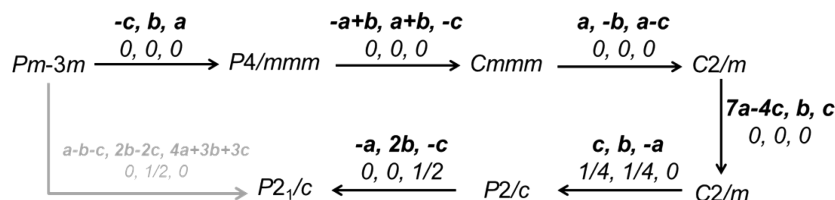
Figure 3. Schematic group−subgroup relationship between the cubic perovskite structure and the monoclinic structure of BaFeO$_{2.5}$.
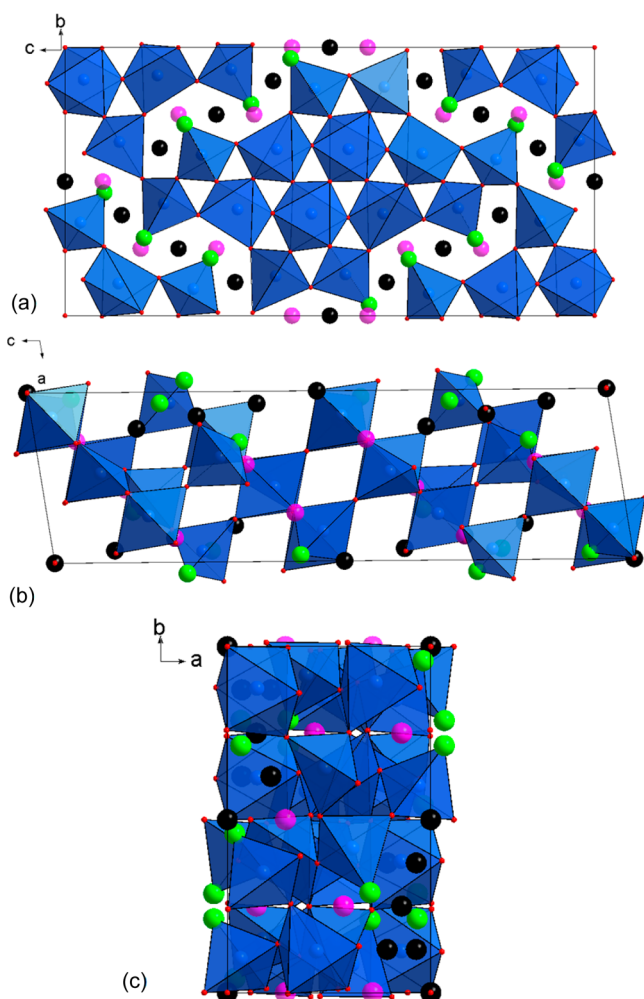
Figure 4. Schematic representation of the location of the vacancies (black balls) in $BaFeO_{2.5}$ (barium ions are not shown). Strongly shifted oxygen ions O2, O3, and O4 are shown as green balls, and the pseudocubic positions of O2, O3, and O4 are shown as purple balls. Viewing directions were chosen along the a (a), b (b), and c (c) axes.

Figure 5. ^{57}Fe Mössbauer spectrum recorded from $BaFeO_{2.5}$ at room temperature.

Table 5. ^{57}Fe **Mössbauer Spectroscopy Parameters (Δ chemical isomer shift, B_{HF} magnetic hyperfine field, ε effective quadrupole interaction parameter) for $BaFeO_{2.5}$ determined from the fit of the spectrum shown in Figure 5**[a]

site	δ [mm s^{-1}]	B_{HF} [T]	ε [mm s^{-1}]	area [%]
Fe7, CN = 6	0.45(1)	50.3(5)	−0.13(2)	13(2)
Fe5, CN = 5	0.37(1)	49.2(5)	−0.50(2)	15(2)
Fe6, CN = 5	0.33(1)	47.3(5)	−0.64(2)	13(2)
Fe1, CN = 4	0.23[c]	42.1(5)	0.63(2)	15(2)
Fe2−4,[b] CN = 4	0.15(1)	40.0(5)	−0.2[c]	44(4)

[a]The values given for the Fe2−4 sites are average values because the component is fitted with a distribution of hyperfine parameters. [b]Tetrahedra for which one corner is not shared with another polyhedron. [c]Parameter is fixed in the refinement.

3.2. Mössbauer Spectroscopic Investigation of $BaFeO_{2.5}$. The ^{57}Fe Mössbauer spectrum recorded from $BaFeO_{2.5}$ at 298 K was best fitted to five components and is shown in Figure 5. The line widths of all components were constrained to 0.35 mm s^{-1}. The parameters are collected in Table 5. The spectrum and fitted parameters are very similar to those reported previously[27] for $BaFeO_{2.5}$. The chemical isomer shifts are all characteristic of Fe^{3+} and are therefore consistent with the formulation $BaFeO_{2.5}$. In addition, the relative areas agree well with the site multiplicities of the different iron sites deduced from structural analysis. The ^{57}Fe Mössbauer chemical isomer shifts are highly dependent on the CN,[51] and the component in the Mössbauer spectrum reported here with a chemical isomer shift of 0.45 mm s^{-1} is consistent with octahedrally coordinated Fe^{3+}. We assign this component to Fe7. This spectral component also shows the largest magnetic hyperfine field, and the chemical isomer shift is similar to that reported for Fe^{3+} in structural variants of the compound $BaFeO_2F$, which also contains Fe^{3+} in octahedral coordination.[14,15,50] The two components with lower chemical isomer shifts of 0.37 and 0.33 mm s^{-1} indicate[51] lower coordination around Fe^{3+}, and we associate these with Fe5 and Fe6 in 5-fold square-pyramidal coordination but in which the sixth oxygen
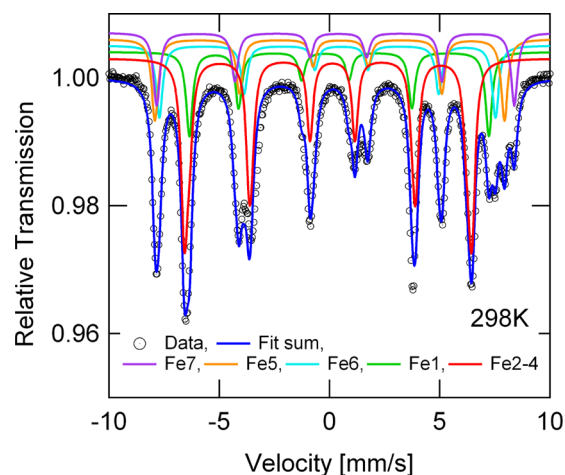
ion at longer distance corresponds to pseudooctahedral coordination. The component with a chemical isomer shift of 0.37 mm s^{-1} is assigned to Fe5, which has a shorter distance to the sixth oxygen ion. We note that our analysis gives lower isomer shifts for the two components with 5-fold coordination compared to the report of Parras et al.[27] (0.45 and 0.44 mm s^{-1}). The components with chemical isomer shifts of 0.23 and 0.15 mm s^{-1} are similar to those of Fe^{3+} in tetrahedral coordination as found in $CaFeO_{2.5}$ and $SrFeO_{2.5}$,[27] and we assign these to the Fe1 and Fe2−4 sites. Among these tetrahedral sites, Fe2−4 are very similar because their tetrahedra possess one corner that is not shared with other iron-containing polyhedra. The unshared oxygen ion in these tetrahedra would be expected to induce a higher degree of covalency in the bonding to Fe^{3+} and lower the chemical isomer shift and magnitude of the magnetic hyperfine field. Hence, we associate the component with a chemical isomer shift of 0.15 mm s^{-1}, B_{HF} = 40 T, and 44% area ratio with Fe2−4. Finally, we associate the component with a chemical isomer shift of 0.23 mm s^{-1} to Fe1, which corresponds to tetrahedrally coordinated Fe^{3+}, where all corners of the tetrahedron are shared with other polyhedra, thereby reducing the degree of covalency in the Fe−O bonds, which is reflected in the more positive chemical isomer shift and larger magnetic hyperfine field. Hence, the ^{57}Fe Mössbauer spectrum reported here, although similar to that described earlier[27] for $BaFeO_{2.5}$, endorses the new structural description proposed here.

3.3. Magnetometric Characterization and Determination of the Magnetic Structure.

$BaFeO_{2.5}$ has been described as a room temperature antiferromagnet with a Néel temperature of 720 K.[27] Magnetization measurements as a function of the applied magnetic field at 5 and 390 K are presented in Figure 6a and show a linear dependence reaching
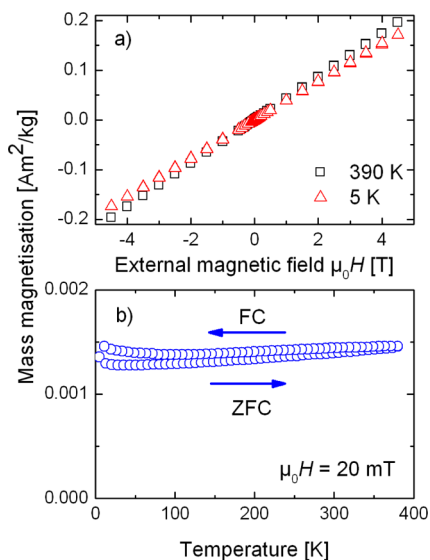

Figure 6. Magnetization measurements as a function of the (a) external magnetic field and (b) temperature.

only very low magnetization values. ZFC/FC measurements (see Figure 6b) exhibit no feature of a magnetic transition or a ferri-/ferromagnetic contribution in the temperature range examined. These observations are in agreement with the antiferromagnetic order determined from the NPD examination of the magnetic structure of $BaFeO_{2.5}$.

Close examination of the NPD data showed the appearance of reflections that cannot be indexed on the basis of the crystallographic unit cell. Therefore, Pawley fits were performed assuming doubling of one of the crystallographic axes (high-resolution backscattering bank of HRPD; d spacing range limited to 1.75−2.55 Å) using the space group $P2$ (no absences of reflections due to translational symmetry). All of the reflections could be indexed on the basis of a cell with $2a_{nuc}$, b_{nuc}, c_{nuc} ($R_{wp} = 7.25\%$), clearly indicating a **k** vector of $[^1/_2, 0, 0]$. In contrast, doubling of the b (**k** = $[0, ^1/_2, 0]$) and c axes (**k** = $[0, 0, ^1/_2]$) ($R_{wp} = 7.97\%$ and 9.01% for the same refinement conditions) did not result in a valid description of the reflections resulting from magnetic scattering, and a Pawley fit using a cell with a_{nuc}, b_{nuc}, and c_{nuc} (**k** = $[0, 0, 0]$) can be clearly discarded for not describing the magnetic reflections properly ($R_{wp} = 12.36$).

G-type antiferromagnetic ordering is often found for antiferromagnetic "cubic perovskite"-type compounds, which contain only Fe^{3+}.[13,45,50,52] This antiferromagnetic ordering is usually enhanced by 180° superexchange coupling (or nearly 180° superexchange, which is found to be the case for $BaFeO_{2.5}$) for corner-sharing Fe−O−Fe polyhedra. Such an antiferromagnetic alignment between neighboring polyhedra enables a G-type antiferromagnetic ordering to be envisaged for the vacancy-ordered variant of $BaFeO_{2.5}$ (see Figure 7). Such an ordering requires a doubling of the a axis of the nuclear cell to describe the magnetic cell, in agreement with the results from
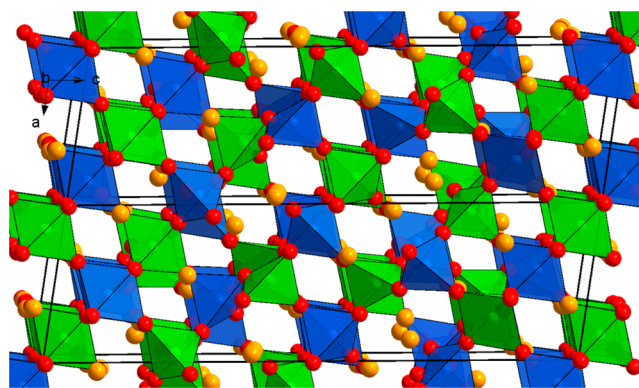

Figure 7. Schematic representation of the magnetic structure of $BaFeO_{2.5}$. Fe^{3+} ions in a spin-up state are found as blue polyhedra, and Fe^{3+} ions in a spin-down state are found as green polyhedra (Ba^{2+} ions, orange; O^{2-} ions, red). The **k** vector with respect to the monoclinic cell is $[^1/_2, 0, 0]$.

the Pawley fit and determined **k** vector of $[^1/_2, 0, 0]$ and indicates that such (or a similar) magnetic ordering might exist in $BaFeO_{2.5}$.

In a first attempt to confirm this G-type order and because only a few reflections resulting from magnetic ordering were present in the NPD data, the magnitude of the magnetic moments of all iron ions were constrained to be the same. In addition, the orientations of the magnetic moments of the iron atoms in polyhedra connected via corners (e.g., Fe_A−O−Fe_B) were constrained in such a way that $M_x(Fe_A) = -M_x(Fe_B)$, $M_y(Fe_A) = -M_y(Fe_B)$, and $M_z(Fe_A) = -M_z(Fe_B)$; i.e., only an overall orientation of the magnetic moments was refined, and only two different overall orientations of the magnetic moment were possible for all of the iron atoms, namely, (M_x, M_y, M_z) and $(-M_x, -M_y, -M_z)$, implying G-type magnetic ordering and in agreement with the overall antiferromagnetic properties. This principal alignment of the magnetic moments would correspond to $P_s\bar{1}$ as the magnetic space group. Several starting orientations of the magnetic moments were examined for this analysis. The best fit to the recorded pattern was obtained for a magnetic moment of $M_x = 1.86 \mu_B$, $M_y = 0.66 \mu_B$, $M_z = 2.99 \mu_B$, and $M_{total} = 3.35(1) \mu_B$, pointing mainly along the c axis, with a very minor contribution of the moment along the b axis.

Despite strict constraints, such an alignment of the magnetic moments already gives a very good description of the intensities resulting from magnetic scattering and therefore indicates that the assumption of G-type ordering for $BaFeO_{2.5}$ is valid. This is also in agreement with the results from the SQUID measurements.

Analyzing the magnetic structure further[53] shows that among the magnetic space groups derived from the Fedorov space group $P2_1/c$, only the magnetic space group P_a2_1/c (BNS 14.80)[54−56] is compatible with a propagation vector of $[^1/_2, 0, 0]$ (see the SI). In total, four magnetic symmetries with space group P_a2_1/c[53] would be possible, which would all be compatible with the overall antiferromagnetic properties of the compound (those symmetries differ with respect to the origin for the antitranslation operation and the choice of the c axis of the cell; see the SI for detailed transformation matrixes). Among them, two settings are, in principle, compatible with G-type ordering of the magnetic moments, one of them allowing for a magnetic moment along the M_x and M_z axes (M_y is then incompatible with G-type ordering) and the other allowing for a magnetic moment along the M_y axis (M_x and M_z are then

incompatible with G-type ordering). The two other settings are not compatible with G-type ordering at all and will result in ferromagnetic alignment of the magnetic moments between at least some of the iron polyhedra connected by corners. We found that only the setting with magnetic moments pointing mainly along the M_x and M_z axes in a G-type ordering (allowing for different magnitudes and directions for the magnetic moments on the different iron sites) can be used to describe the magnetic reflections properly (also see the SI). This was also already indicated by the refinement using space group $P_s\bar{1}$, where M_y is the weakest among the three different crystallographic directions (this component therefore has only a minor influence on the quality of the fit of the magnetic reflections). The final refinement using space group P_a2_1/c, shown in Figure 1 (with $M_y = 0$), results in an almost equally good fit of the diffraction pattern ($\Delta R_{wp} \sim 0.01$) compared to that using the P_a2_1/c setting without fixing M_y to 0, confirming the alignment of the magnetic moments in the ac plane. Furthermore, the magnetic space group P_a2_1/c is also maximal; i.e., a propagation vector of $[^1/_2, 0, 0]$ would not allow for any magnetic ordering with higher symmetry. The magnetic structure is included in a cif-like file (mcif format), which is supported by programs like ISODISTORT,[57] VESTA,[58] etc., in the SI.

The magnetic moments for the different iron sites are listed in Table 6. The magnetic moment increases with the CN by

Table 6. Magnetic Moments for the Different Crystallographic Sites Determined from Rietveld Analysis of the Magnetic Structure of $BaFeO_{2.5}$[a]

site	CN	M_x [μ_B]	M_z [μ_B]	M_{total} [μ_B]
Fe1	4	2.4(2)	3.4(1)	3.8
Fe2*	4	−1.9(2)	−2.6(1)	3.0
Fe3*	4	1.6(2)	2.4(1)	2.6
Fe4*	4	1.9(2)	2.9(1)	3.2
Fe5	5	−2.4(2)	−3.3(1)	3.8
Fe6	5	−1.4(2)	−3.6(1)	3.7
Fe7	6	1.3(2)	4.2(1)	4.2

[a]* = one corner of the coordination tetrahedron is not properly shared with a neighbouring polyhedron.

trend, and this agrees well with the fact that the magnetic moment obtained from NPD is lowered if covalent bonding is present (which is stronger for shorter Fe−O bonds, i.e., lower CNs). Among the four tetrahedrally coordinated iron atoms, the magnetic moments for Fe2−4 are significantly lower than the one for Fe1, and those iron atoms are connected to one oxygen ion, which is not shared with another iron coordination polyhedron. This trend is also confirmed regarding the magnetic hyperfine fields obtained from the fit of the Mössbauer spectrum (see Table 5, section 3.2) and from the behavior of the pDOS reported in the following section. Furthermore, the overall magnitude of the magnetic moments agrees well with that found for similar perovskite-type compounds also containing mainly/only Fe^{3+}[14,15,45,59] and showing magnetic order at room temperature. Because of the high correlation and small number of magnetic reflections, we think the small canting of magnetic moments between neighboring sites should not be overinterpreted.

3.4. DFT-Based Optimization of the Crystallographic and Electronic Structure. DFT-based calculations showed only very small changes in the local coordination environments of the iron atoms, i.e., small changes (e.g., <0.09 Å in the bond

distances for the Fe−O bonds), same principal coordination and very similar lattice parameters (a = 6.957 Å, b = 11.759 Å, c = 23.409 Å, and β = 98.28°). Overall, the DFT calculations give a good indication that the structural arrangement from analysis of the XRD and NPD data can be considered to be stable; i.e., no square-pyramidal coordination changed into octahedral coordination.

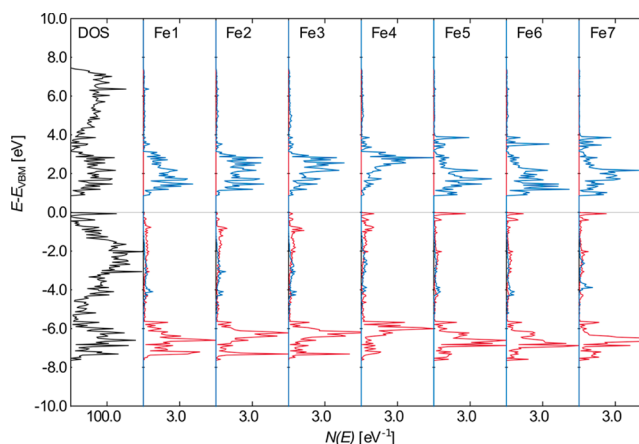The density of states (DOS) and pDOS of the seven crystallographically different iron atoms are plotted in Figure 8.

Figure 8. Total DOS and pDOS for the different iron sites in $BaFeO_{2.5}$.

Comparing the pDOS for the tetrahedrally coordinated iron atoms Fe1−4, one can see that the center of gravity of the states of Fe1 is shifted to lower energies compared to Fe2−4. This can be explained by the fact that all of the oxygen ions connected to Fe1 are properly shared with other iron atoms, whereas Fe2−4 each have one oxygen atom that is not shared with other polyhedra.

Among them, the pDOS of Fe4 is again slightly different because of the fact that its outstanding oxygen is pointing toward the face of the coordination tetrahedron of Fe2, whereas for Fe2 and Fe3, the free-standing oxygen could be considered slightly bonded to Fe5 with respect to the Fe6 atom. Therefore, Fe4 should be more covalently bonded to its free-standing oxygen than in the situation with Fe2 + Fe3. This is also reflected in the Mössbauer data attributed to the tetrahedral sites (see section 3.3), with Fe1 having a more positive and Fe2−4 a slightly reduced isomer shift.

The pDOSs of the octahedral/square-pyramidal sites for Fe5, Fe6, and Fe7 are rather similar and again with different centers of gravities for the occupied states. The pDOS for Fe7, which shows proper octahedral coordination, again looks slightly different compared to the pDOSs of Fe5 and Fe6, with the center of gravity of the occupied states shifted to slightly higher energies for Fe7. Overall, we can conclude that the behavior of the isomer shifts recorded by Mössbauer spectroscopy agrees well with the results from the DFT-based calculations.

4. CONCLUSION

We show here that the crystal structure of monoclinic $BaFeO_{2.5}$ can be understood in terms of a highly complex vacancy-ordered modification of the cubic perovskite structure. This structure is, to our knowledge, the least symmetric vacancy-ordered perovskite so far reported, containing seven crystallographically different iron ions. Solving the structure was only

possible by the use of high-resolution NPD data in combination with laboratory XRD data. The structure contains iron in octahedral (1/7), square-pyramidal (2/7), and tetrahedral (4/7) coordination. The compound shows antiferromagnetic ordering at room temperature. Although the crystallographic structure is highly complicated, the magnetic structure can be understood in terms of a simple G-type antiferromagnetic ordering, being in agreement with FC/ZFC and field-sweep measurements.

■ ASSOCIATED CONTENT

Ⓢ Supporting Information

Symmetry relationship between the cubic perovskite and monoclinic distortion found, EDX analysis, SEM images, determination of the degree of crystallinity, magnetic symmetry relationships, and a cif and a mcif file containing the crystallographic data. This material is available free of charge via the Internet at http://pubs.acs.org.

■ AUTHOR INFORMATION

Corresponding Author

*Fax: +49 6151 16 6335. E-mail: oliver.clemens@kit.edu.

Notes

The authors declare no competing financial interest.

■ ACKNOWLEDGMENTS

■ REFERENCES

(1) Benel, C.; Darbandi, A. J.; Djenadic, R.; Evans, A.; Tölke, R.; Prestat, M.; Hahn, H. *J. Power Sources* **2013**, *229*, 258−264.

(2) Mizusaki, J.; Sasamoto, T.; Cannon, W. R.; Bowen, H. K. *J. Am. Ceram. Soc.* **1983**, *66*, 247−252.

(3) Deng, G.; Chen, Y.; Tao, M.; Wu, C.; Shen, X.; Yang, H. *Electrochim. Acta* **2009**, *54*, 3910−3914.

(4) Harada, J.; Pedersen, T.; Barnea, Z. *Acta Crystallogr.* **1970**, *26*, 336−344.

(5) Teague, J. R.; Gerson, R.; James, W. J. *Solid State Commun.* **1970**, *8*, 1073−1074.

(6) Sosnowska, I.; Peterlin-Neumaier, T.; Steichele, E. *J. Phys. C: Solid State Phys.* **1982**, *15*, 4835−4846.

(7) Neaton, J. B.; Ederer, C.; Waghmare, U. V.; Spaldin, N. A.; Rabe, K. M. *Phys. Rev. B* **2005**, *71*, 014113.

(8) Khomchenko, V. A.; Kiselev, D. A.; Vieira, J. M.; Kholkin, A. L.; Sa, M. A.; Pogorelov, Y. G. *Appl. Phys. Lett.* **2007**, *90*, 242901.

(9) Khomchenko, V. A.; Kiselev, D. A.; Seluneva, E. K.; Vieira, J. M.; Lopes, A. M. L.; Pogorelov, Y. G.; Araujo, J. P.; Kholkin, A. L. *Mater. Lett.* **2008**, *62*, 1927−1929.

(10) Catalan, G.; Scott, J. F. *Adv. Mater. (Weinheim, Ger.)* **2009**, *21*, 2463−2485.

(11) Masó, N.; West, A. R. *Chem. Mater.* **2012**, *24*, 2127−2132.

(12) Hayashi, N.; Yamamoto, T.; Kageyama, H.; Nishi, M.; Watanabe, Y.; Kawakami, T.; Matsushita, Y.; Fujimori, A.; Takano, M. *Angew. Chem., Int. Ed.* **2011**, *50*, 12547−12550.

(13) Heap, R.; Slater, P. R.; Berry, F. J.; Helgason, O.; Wright, A. J. *Solid State Commun.* **2007**, *141*, 467−470.

(14) Clemens, O.; Berry, F. J.; Bauer, J.; Wright, A. J.; Knight, K. S.; Slater, P. R. *J. Solid State Chem.* **2013**, *203*, 218−226.

(15) Clemens, O.; Wright, A. J.; Berry, F. J.; Smith, R. I.; Slater, P. R. *J. Solid State Chem.* **2013**, *198*, 262−269.

(16) Colville, A. A.; Geller, S. *Acta Crystallogr., Sect. B* **1971**, *27*, 2311−2315.

(17) Clemens, O.; Slater, P. R. *Rev. Inorg. Chem.* **2013**, *33*, 105−117.

(18) Schmidt, M.; Campbell, S. J. *J. Solid State Chem.* **2001**, *156*, 292−304.

(19) Berastegui, P.; Eriksson, S. G.; Hull, S. *Mater. Res. Bull.* **1999**, *34*, 303−314.

(20) Berastegui, P.; Hull, S.; García-García, F. J.; Eriksson, S. G. *J. Solid State Chem.* **2002**, *164*, 119−130.

(21) Muñoz, A.; de la Calle, C.; Alonso, J. A.; Botta, P. M.; Pardo, V.; Baldomir, D.; Rivas, J. *Phys. Rev. B* **2008**, *78*, 054404.

(22) Abakumov, A. M.; Rozova, M. G.; Pavlyuk, B. P.; Lobanov, M. V.; Antipov, E. V.; Lebedev, O. I.; Van Tendeloo, G.; Sheptyakov, D. V.; Balagurov, A. M.; Bourée, F. *J. Solid State Chem.* **2001**, *158*, 100−111.

(23) Stolen, S.; Bakken, E.; Mohn, C. E. *Phys. Chem. Chem. Phys.* **2006**, *8*, 429−447.

(24) Anderson, M. T.; Vaughey, J. T.; Poeppelmeier, K. R. *Chem. Mater.* **1993**, *5*, 151−165.

(25) Mori, S. *J. Am. Ceram. Soc.* **1966**, *49*, 600−605.

(26) Parras, M.; Vallet-Regi, M.; Gonzalez-Calbet, J. M.; Alario-Franco, M. A.; Grenier, J. C.; Hagenmuller, P. *Mater. Res. Bull.* **1987**, *22*, 1413−1419.

(27) Parras, M.; Fournes, L.; Grenier, J. C.; Pouchard, M.; Vallet, M.; Calbet, J. M.; Hagenmuller, P. *J. Solid State Chem.* **1990**, *88*, 261−268.

(28) Zou, X. D.; Hovmoller, S.; Parras, M.; Gonzalez-Calbet, J. M.; Vallet-Regi, M.; Grenier, J. C. *Acta Crystallogr., Sect. A* **1993**, *49*, 27−35.

(29) Fujishiro, F.; Fukasawa, K.; Hashimoto, T. *J. Am. Ceram. Soc.* **2011**, *94*, 3675−3678.

(30) Fujishiro, F.; Kojima, Y.; Hashimoto, T. *J. Am. Ceram. Soc.* **2012**, *95*, 3634−3637.

(31) Clemens, O.; Hahn, H.; Slater, P. R., in preparation.

(32) *Topas V4.2, General profile and structure analysis software for powder diffraction data, User's Manual*; Bruker AXS: Karlsruhe, Germany, 2008.

(33) Cheary, R. W.; Coelho, A. A.; Cline, J. P. *J. Res. Natl. Inst. Stand. Technol.* **2004**, *109*, 1−25.

(34) Coelho, A. A. *TOPAS-Academic*, http://www.topas-academic.net, 2004.

(35) Brand, R. A.; Lauer, J.; Herlach, D. M. *J. Phys. F: Met. Phys.* **1983**, *13*, 675.

(36) Kresse, G.; Hafner, J. *Phys. Rev. B* **1993**, *47*, 558.

(37) Kresse, G.; Hafner, J. *Phys. Rev. B* **1994**, *49*, 14251.

(38) Kresse, G.; Furthmüller, J. *Comput. Mater. Sci.* **1996**, *6*, 15.

(39) Kresse, G.; Furthmüller, J. *Phys. Rev. B* **1996**, *54*, 11169.

(40) Kresse, G.; Joubert, D. *Phys. Rev. B* **1999**, *59*, 1758.

(41) Perdew, J. P.; Burke, K.; Ernzerhof, M. *Phys. Rev. Lett.* **1996**, *77*, 3865.

(42) Dudarev, S. L.; Botton, G. A.; Savrasov, S. Y.; Humphreys, C. J.; Sutton, A. P. *Phys. Rev. B* **1998**, *57*, 1505.

(43) Kornev, I. A.; Lisenkov, S.; Haumont, R.; Dkhil, B.; Bellaiche, L. *Phys. Rev. Lett.* **2007**, *99*, 227602.

(44) Shannon, R. D. *Acta Crystallogr.* **1976**, *A32*, 751−767.

(45) Clemens, O.; Berry, F. J.; Wright, A. J.; Knight, K. S.; Perez-Mato, J. M.; Igartua, J. M.; Slater, P. R. *J. Solid State Chem.* **2013**, *206*, 158−169.

(46) Darlington, C. N. W.; David, W. I. F.; Knight, K. S. *Phase Transitions* **1994**, *48*, 217−236.

(47) Brown, I. D.; Wu, K. K. *Acta Crystallogr., Sect. B* **1976**, *32*, 1957−1959.

(48) Hoppe, R. *Z. Kristallogr.* **1979**, *150*, 23−52.

(49) Clemens, O.; Haberkorn, R.; Slater, P. R.; Beck, H. P. *Solid State Sci.* **2010**, *12*, 1455−1463.

(50) Berry, F. J.; Coomer, F. C.; Hancock, C.; Helgason, Ö.; Moore, E. A.; Slater, P. R.; Wright, A. J.; Thomas, M. F. *J. Solid State Chem.* **2011**, *184*, 1361−1366.

(51) Menil, F. *J. Phys. Chem. Solids* **1985**, *46*, 763−789.

(52) Berry, F. J.; Heap, R.; Helgason, Ö.; Moore, E. A.; Shim, S.; Slater, P. R.; Thomas, M. F. *J. Phys.: Condens. Matter* **2008**, *20*, 215207.

(53) MAXMAGN in the Bilbao Crystallographic Server, http://cryst.ehu.es.

5920

dx.doi.org/10.1021/ic402988y | *Inorg. Chem.* 2014, 53, 5911−5921

(54) Gallego, S. V.; Tasci, E. S.; de la Flor, G.; Perez-Mato, J. M.; Aroyo, M. I. *J. Appl. Crystallogr.* **2012**, *45*, 1236−1247.

(55) MGENPOS in the Bilbao Crystallographic Server, http://cryst. ehu.es.

(56) Stokes, H. T.; Campbell, B. J., http://stokes.byu.edu/ magneticspacegroups.html, 2011.

(57) Campbell, B. J.; Stokes, H. T.; Tanner, D. E.; Hatch, D. M. *J. Appl. Crystallogr.* **2006**, *39*, 607−614.

(58) Momma, K.; Izumi, F. *J. Appl. Crystallogr.* **2011**, *44*, 1272−1276.

(59) Sturza, M.; Kabbour, H.; Daviero-Minaud, S.; Filimonov, D.; Pokholok, K.; Tiercelin, N.; Porcher, F.; Aldon, L.; Mentre, O. *J. Am. Chem. Soc.* **2011**, *133*, 10901−10909.

5921

dx.doi.org/10.1021/ic402988y | *Inorg. Chem.* 2014, 53, 5911−5921